

www.acsami.org Research Article

# Graphene-like Vanadium Oxygen Hydrate (VOH) Nanosheets Intercalated and Exfoliated by Polyaniline (PANI) for Aqueous Zinclon Batteries (ZIBs)

Mingshan Wang,\* Jun Zhang, Linzi Zhang, Jiaqi Li, Wenjie Wang, Zhenliang Yang, Lei Zhang, Yixian Wang, Junchen Chen, Yun Huang, David Mitlin,\* and Xing Li\*



Cite This: ACS Appl. Mater. Interfaces 2020, 12, 31564-31574



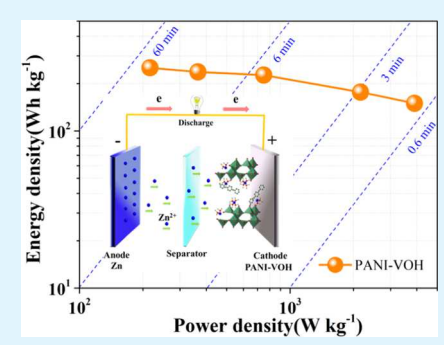
ACCESS

Metrics & More

Article Recommendations

Supporting Information

**ABSTRACT:** A new approach is employed to boost the electrochemical kinetics and stability of vanadium oxygen hydrate (VOH,  $V_2O_5 \cdot nH_2O$ ) employed for aqueous zincion battery (ZIB) cathodes. The methodology is based on electrically conductive polyaniline (PANI) intercalated—exfoliated VOH, achieved by preintercalation of an aniline monomer and its *in situ* polymerization within the oxide interlayers. The resulting graphene-like PANI—VOH nanosheets possess a greatly boosted reaction-controlled contribution to the total charge storage capacity, resulting in more material undergoing the reversible V<sup>5+</sup> to V<sup>3+</sup> redox reaction. The PANI—VOH electrode obtains an impressive capacity of 323 mAh g<sup>-1</sup> at 1 A g<sup>-1</sup>, and state-of-the-art cycling stability at 80% capacity retention after 800 cycles. Because of the facile redox kinetics, the PANI—VOH ZIB obtains uniquely promising specific energy—specific power combinations: an energy of 216 Wh kg<sup>-1</sup> is achieved at 252 W kg<sup>-1</sup>, while 150 Wh kg<sup>-1</sup> is achieved at 3900



W kg $^{-1}$ . Electrochemical impedance spectroscopy (EIS) and galvanostatic intermittent titration technique (GITT) analyses indicate that with PANI–VOH nanosheets, there is a simultaneous decrease in the charge transfer resistance and a boost in the diffusion coefficient of Zn $^{2+}$  (by a factor of 10–100) vs the VOH baseline. The strategy of employing PANI for combined intercalation–exfoliation may provide a broadly applicable approach for improving the performance in a range of oxide-based energy storage materials.

KEYWORDS: vanadium pentoxide V<sub>2</sub>O<sub>5</sub>, vanadium oxide cathode, aqueous ion battery, sodium vanadate cathode, zinc metal anode

## 1. INTRODUCTION

Although lithium-ion batteries (LIBs) are showing remarkable growth and market dominance in automotive and portable applications, there is a need for less costly and more safe battery systems based on earth-abundant elements. Aqueous secondary batteries based on metal ions, including Na+, K+,  $Mg^{2+}$ ,  $Zn^{2+}$ ,  $Ca^{2+}$ , and  $Al^{3+}$ ,  $Z^{2-8}$  possess multiple advantages, including the natural abundance of potential cathode and anode materials, high fire safety, and low system cost, potentially making them suitable for stationary and grid-scale energy storage applications. 9-13 Aqueous zinc-ion batteries (ZIBs) possess a relatively high theoretical energy due to the Zn anode  $(Zn/Zn^{2+} = 820 \text{ mAh g}^{-1}, -0.76 \text{ V } vs \text{ H}_2/\text{H}^+)$ , and are safe and inexpensive. Therefore, ZIBs are considered among the most promising aqueous systems and potential alternatives to LIBs. The original ZIB was the Zn-MnO<sub>2</sub> battery, published by Shoji et al. in 1986.<sup>14</sup> It consisted of a Zn metal anode, a MnO<sub>2</sub> cathode, and a neutral ZnSO<sub>4</sub> aqueous solution as the electrolyte. The cathode material was chosen as α-MnO<sub>2</sub> because of its tunnel structure, which can provide sufficient channels for Zn<sup>2+</sup> intercalation/extraction. During cycling, however, this structure underwent irreversible phase

conversion and manganese dissolution, leading to a dramatic capacity fade.  $^{15}$  Following these steps, researchers have focused on discovering suitable cathode materials to obtain long-term cyclability in ZIBs. Although the ionic radius of  $\mathrm{Zn^{2+}}$  is relatively small, there are strong electrostatic repulsion forces when intercalating host crystalline structures, resulting in shortcomings in rate kinetics and cyclability. An ideal cathode material would contain a large channel structure to facilitate the reversible intercalation/extraction of  $\mathrm{Zn^{2+}}$ .

Vanadium-based oxides are among the most promising cathode materials for ZIBs due to the polyvalent vanadium ions (+5, +4, +3, +2), which can realize multielectron transfer with a high reversible capacity between 300 and 400 mAh  $g^{-1}$ . Vanadium-based oxides and their derivatives are important compounds used in lithium-ion battery and

Received: June 4, 2020 Accepted: June 17, 2020 Published: June 17, 2020





sodium-ion battery research, 16-18 meaning that there a significant body of scientific understanding regarding their structure and synthesis. Current research regarding vanadiumbased oxides for ZIBs includes vanadium pentoxide  $(V_2O_5)$ ,  $^{19,20}$  vanadium oxide  $(V_6O_{13})$ ,  $^{21}$  vanadium oxygen hydrate  $(V_2O_5 \cdot nH_2O)$ , vanadate  $(NaV_3O_8 \cdot 1.5H_2O)$ , AgVO, E(x), E(x), and other derivatives. Among them, V<sub>2</sub>O<sub>5</sub> is a typical vanadium-based compound with a layered structure. The V atom and the O atom are five-coordinated, forming a [VO<sub>5</sub>] quadric pyramid, further connecting with each other by common edges. The adjacent layers are connected by van der Waals forces, making it suitable for the reversible insertion of  $Zn^{2+}$ . The earliest  $V_2O_5$  as a ZIB cathode material was put forward by Johnson et al., based on a V<sub>2</sub>O<sub>5</sub>II Zn architecture.<sup>20</sup> However, its first discharge-specific capacity was limited to 196 mAh g<sup>-1</sup>, due to the narrow layer spacing of the adjacent V–O layers and insufficient  $\mathrm{Zn}^{2+}$  diffusivity. In turn, expanding the interlayer distance by substituting other metal ions into the structure, such as Zn2+, Ca2+, Ag+, etc., to form  $Zn_{0.25}V_2O_5 \cdot nH_2O$ ,  $Ca_{0.25}V_2O_5 \cdot nH_2O$ , and  $Ag_{0.4}V_2O_5$ , is an effective approach for enhancing Zn<sup>2+</sup> diffusivity.

Another strategy to improve Zn<sup>2+</sup> diffusion kinetics in V<sub>2</sub>O<sub>5</sub> is to preintercalate water molecules into the V-O layers to form vanadium oxygen hydrate (VOH). The diffusivity of Zn<sup>2+</sup> within the more open structure of the hydrate is faster than in anhydrous V<sub>2</sub>O<sub>5</sub>, leading to improved redox kinetics. However, during the repeated insertion/extraction of Zn<sup>2+</sup>, the intercalated water molecules tend to come out of the interlayers, which ultimately leads to the collapse of the layered structure. Taking advantage of the above methods, some research studies have combined the approaches, preintercalating metal ions into VOH to synergistically increase the stability of the layered structure. The results show the metal ion-preintercalared VOH with improved kinetics and stability, including Zn<sub>0.25</sub>V<sub>2</sub>O<sub>5</sub>·nH<sub>2</sub>O and Ca<sub>0.25</sub>V<sub>2</sub>O<sub>5</sub>·nH<sub>2</sub>O.<sup>5,7</sup> In such structures, most hetero metal ions are redox inactive, which will reduce the overall reversible capacity of the compounds.

Here, we developed a new approach to boost the kinetics and cyclability of VOH cathodes for aqueous ZIBs. The highperformance cathode material is polyaniline (PANI) intercalated and exfoliated VOH, termed "PANI-VOH". It was prepared by preintercalating an aniline monomer into the interlayers of VOH, followed by in situ polymerization. The relatively simple low-temperature process results in the longchain structure of PANI, further exfoliating VOH into nanosheets that resemble a few-layers of graphene. These VOH nanosheets along with PANI provide abundant active sites for reversible Zn<sup>2+</sup> storage, resulting in a substantial reaction-controlled (termed "capacitive") contribution to the overall capacity. The cycling stability of PANI-VOH is also significantly improved over the VOH baseline. The details for the relationship between the structure of PANI-VOH, its electrochemical performance, and the associated redox mechanisms are investigated and discussed.

## 2. EXPERIMENTAL SECTION

**2.1. Synthesis of PANI–VOH.** The aniline (AN) monomer (99%) was purchased from Aladdin Co. Ltd. HCl (36.0–38.0%) and  $\rm H_2O_2$  were purchased from Chengdu Kelong Co. Ltd., and  $\rm V_2O_5$  (99.6%) was purchased from Alfa Aesar. All of the chemical reagents were directly used without purification. PANI–VOH was synthesized through a low-temperature chemical method. First, 2 mmol of  $\rm V_2O_5$ 

was added to 80 mL of deionized water with the addition of 2 mL of  $\rm H_2O_2$ . After stirring for 1 h at room temperature, a red solution was obtained. Next, 0.8 mmol AN was added into 150 mL of deionized water. The acidity of the AN solution was adjusted using 1 M HCl to obtain pH 2. After strong agitation, the  $\rm V_2O_5$  aqueous solution was added into the AN solution and held at 120 °C for 3 h. After this, the precipitate was centrifuged and collected, followed by several iterations of washing with deionized water. Finally, dark green solids were obtained by freeze-drying for 48 h to remove the water. Baseline VOH was synthesized through a comparable approach but without adding AN.

**2.2. Material Characterization.** X-ray diffraction (XRD) analysis was performed using a PANalytical X'Pert Pro diffractometer with Cu  $K\alpha$  radiation ( $\lambda$  = 1.5406 Å). Thermogravimetric analysis (TGA) was performed using the Netzsch STA 449F3 analyzer in air, with a ramp rate of 10 °C min<sup>-1</sup>. Raman spectroscopy analysis was carried out using the Renishaw RM 1000-Invia  $\lambda$  = 785 nm with the wavenumber ranging from 100 to 2000 cm<sup>-1</sup>. Fourier-transform infrared (FTIR) spectra were acquired on a Nicolet 6700 FTIR Spectrometer. X-ray photoelectron spectroscopy (XPS) analysis was conducted using PHIS000 Versa Probe III with Al  $K\alpha$  radiation. Nitrogen adsorption/desorption isotherms were obtained using the Quadrasorb SI analyzer at 77 K. The morphologies of the samples were characterized by the field-emission scanning electron microscopy (FE-SEM) (FEI INSPECT-F, 20 kV) and high-resolution transmission electron microscopy (HRTEM) (Tecnai G2 F20 S-TWIN, 200 kV).

**2.3. Electrochemical Analysis.** Coin cell batteries (2032-type) were assembled in an air atmosphere for electrochemical investigation. PANI-VOH and VOH electrodes were prepared by coating a mixed slurry (active material, acetylene black, and a PVDF binder with a mass ratio of 7:2:1) on titanium foil. The mass loading of the PANI-VOH and VOH cathodes on the current collector was in the 1.8-2.0 mg cm<sup>-2</sup> range. Prior to being placed into the coin cells, the electrodes were dried in a vacuum oven at 70 °C for 12 h. A standard laboratory-grade zinc foil was used as the anode. Glass fibers (GF/A) were used as separators, and a solution of 3 M zinc trifluoromethyl mesylate (Zn(TfO)<sub>2</sub>) + 6 M trifluoromethyl sulfimide lithium (LiTFSI) was utilized as the electrolyte. LiTFSI (6 M) is added to the Zn(TfO)<sub>2</sub> electrolyte to create a water-in-salt structure. <sup>25</sup> Such an electrolyte enables an additional release of zinc ions while depositing Zn<sup>2+</sup> from solution, improving the overall cell stability, including the Coulombic efficiency (CE). At the same time, such a high concentration kinetically suppresses the thermodynamic decomposition of water during cycling. Galvanostatic charge-discharge testing and galvanostatic intermittent titration technique (GITT) analyses were carried out using Neware workstation at a current density of 50 mA g<sup>-1</sup> and a charge/discharge time and interval of 800 s for each step. Tests were conducted in the voltage range of 0.4-1.6 V, with current densities ranging from 0.3 to 5.0 A g-1. CHI760 Shanghai ChenHua workstations were utilized to perform the cyclic voltammogram (CV) testing, using the voltage range of 0.4-1.6~V with a scanning rate of  $0.1~mV~s^{-1}$ . Electrochemical impedance spectroscopy (EIS) measurements were conducted in the frequency range of  $10^{-2}$ 10<sup>5</sup> Hz with the AC amplitude of 5 mV.

## 3. RESULTS AND DISCUSSION

Figure 1 shows characterization results of the as-synthesized PANI–VOH and baseline VOH microstructures. Figure 1a compares the XRD results for PANI–VOH and VOH. It can be seen that the diffraction peaks in both materials correspond to the theoretical main diffraction peaks of VOH (PDF No. 25-1006). In the baseline VOH, the (002) peak is at  $6.66^{\circ}$ , corresponding to a layer spacing of 13.1 Å. This indicates that the intercalated water molecules have enlarged the layer spacing from 10.6 Å for anhydrous  $V_2O_5^{\ 26}$  The (002) peak of PANI–VOH is at  $6.24^{\circ}$ , with an even larger layer space of 14.2 Å. The presence of PANI in PANI–VOH was confirmed by TG and FTIR analyses. As shown in Figure S1, it was found

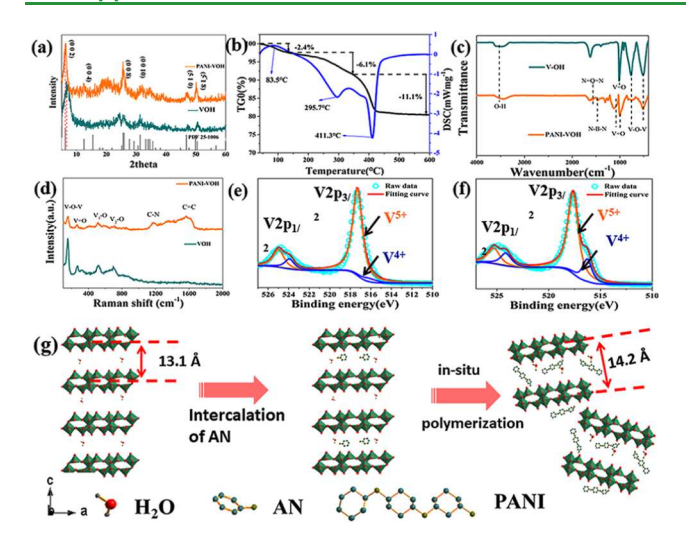


**Figure 1.** (a) XRD patterns of the as-synthesized PANI–VOH and baseline VOH. (b) TGA–DSC profile of PANI–VOH heated in air. (c) FTIR spectra of PANI–VOH and VOH. (d) Raman spectra of PANI–VOH and VOH. High-resolution V  $2p_{1/2}$  and V  $2p_{3/2}$  XPS spectra for (e) VOH and (f) PANI–VOH. (g) Schematic illustration of the fabrication process for PANI–VOH.

that there is a significant weight loss (8.3%) below 150 °C, which correlates with the loss of water molecules adsorbed on VOH surfaces, rather than incorporated into the structure. The secondary weight loss of 3% occurs at the temperature ranging between 150 and 350 °C, corresponding to the loss of water within the VOH structure.<sup>27</sup> It can be calculated that the molar ratio of water in VOH is about 0.3 so that the molecular structure of VOH can be considered as V<sub>2</sub>O<sub>5</sub>·0.3H<sub>2</sub>O. As shown in Figure 1b, there is a 6.1% weight loss that occurs between 150 and 350 °C for PANI-VOH, more than twice compared to that for VOH. This signifies that there is a strong interaction of PANI with the bound water molecules. For PANI-VOH, there is an additional 11.1% weight loss that occurs between 350 and 600 °C. The thermal loss in this hightemperature range is attributed to the thermal decomposition of PANI in air. 28,29 Therefore, the weight content of PANI in PANI-VOH is calculated to be around 11%.

Figure 1c compares the FTIR spectra for VOH and PANI-VOH. The main infrared absorption peaks of VOH appear at 3483, 1617, 1014, 765, and 507 cm<sup>-1</sup>, respectively. The peaks located at 3483 and 1617 cm<sup>-1</sup> are indexed to the vibration of hydroxyl in water, coming from the overlap of O-H for the structural and absorbed water in VOH. The peak located at 1014 cm<sup>-1</sup> is ascribed to the vibration response of V=O in VOH. The two peaks at 765 and 507 cm<sup>-1</sup> represent the characteristic absorption peaks of the V-O-V ring.<sup>30</sup> After the introduction of PANI, the characteristic absorption vibration of O-H binding coming from water (3430/1612 cm<sup>-1</sup>) red shifts about 53/5 cm<sup>-1</sup> compared to the absorption peak in VOH. This means that the H-O binding energy of H<sub>2</sub>O becomes weaker in PANI-VOH. This demonstrates that there is a strong hydrogen bond interaction between H- of H<sub>2</sub>O and PANI-VOH due to the presence of PANI. For PANI-VOH, the additional absorption vibration peaks appear at 1566, 1467, 1303, 1112, and 1057 cm<sup>-1</sup>. Among them, at 1566 and 1467 cm  $^{-1}$  are the characteristic absorption peaks of quinone (N= Q=N) and benzene (N-B-N) structures from PANI, respectively.<sup>28</sup> The peaks at 1303 and 1112 cm<sup>-1</sup> represent the stretching vibration of C-N and the bending vibration of aromatic C-H.<sup>31</sup> The appearance of these peaks directly confirms the polymerization of AN within the VOH layers. For PANI-VOH, the V=O peak in VOH at 1014 cm<sup>-1</sup> splits into two peaks (995 and 1064 cm<sup>-1</sup>). This means that there is an interaction between -NH<sup>3+</sup> of PANI and V=O, giving further evidence for *in situ* polymerization.<sup>32</sup>

Figure 1d shows a comparison of the Raman spectra of VOH and PANI–VOH. Both spectra show a strong characteristic peak located at 153 cm<sup>-1</sup>, indexed as the V–O–V chain in the VOH structure. For PANI–VOH, there are characteristic C–H, C–N, and C=C vibration peaks at 1179, 1257/1350, and 1564 cm<sup>-1</sup>, associated with PANI.<sup>33,34</sup> The relative intensity of V–O–V peaks in PANI–VOH is weaker than those of VOH. A characteristic peak from V=O appears at 268 cm<sup>-1</sup> and blue shifts 3 cm<sup>-1</sup> in PANI–VOH. This agrees with the FTIR results, where there is a split in the absorption peak. The Raman spectra show a stretching signal peak at 519 cm<sup>-1</sup> and a vibration peak at 695 cm<sup>-1</sup>, correlated to V<sub>3</sub>–O and V<sub>2</sub>–O, respectively.<sup>30,35,36</sup> In PANI–VOH, these peaks are relatively weaker than those of in VOH, nominally due to the intercalation of PANI.

The bonding characteristics of VOH and PANI-VOH were further evaluated by XPS. Figure 1e,f compares the V 2p<sub>1/2</sub> and V 2p<sub>3/2</sub> spectra of VOH and PANI-VOH, respectively. There are two typical peaks in the energy range of 512-527 eV, which are ascribed to the  $V^{5+}$  and  $V^{4+}$  species, respectively. This indicates that V5+ is partly reduced in both VOH and PANI-VOH. However, the peak intensity of V<sup>4+</sup> in PANI-VOH is much higher than VOH, indicating more reduction of  $V^{5+}$  to  $V^{4+}$  by the AN.  $^{34,37}$  Moreover, the binding energy of  $V^{5+}$ for PANI-VOH blue shifts 0.3 eV, revealing the change of the electron delocalization for V atoms from V-O layers after the introduction of PANI.<sup>30</sup> From the above results, one can provide a general description of the chemical changes that occur during the synthesis process of PANI-VOH. Figure 1g provides a schematic of this reaction, where the protonated aniline (aniline-H<sup>+</sup>) along with the water molecules is intercalated in the V<sub>2</sub>O<sub>5</sub> interlayers, being attracted to VO<sub>3</sub> by the electrostatic assembly. Then, monoaniline-H<sup>+</sup> in situ polymerizes to long-chain PANI, the process being catalyzed by V<sub>2</sub>O<sub>5</sub>. During this process, the V-O interlayers are further expanded and exfoliated.

PANI-VOH displays a significant morphology difference compared to VOH. As shown in Figure S2, VOH exhibits a thick two-dimensional structure. According to SEM analysis shown in Figure 2a, VOH displays a relatively smooth surface, indicating minimal exfoliation by the water molecules. By contrast, PANI-VOH exhibits a corrugated surface that is full of pores. This is a typical surface morphology that results from gas evolution during an in situ reaction, likely occurring during the combined intercalation-polymerization process. SEM analysis results for PANI-VOH are shown in Figure 2b. The N<sub>2</sub> adsorption/desorption curves of PANI-VOH are shown in Figure S3a. The curves display Type IV isotherms with H4 hysteresis loops. According to the BET test results (Table S1), PANI-VOH possesses a higher  $S_{\rm BET}$  than VOH, at 62.45 vs 2.53 m<sup>2</sup> g<sup>-1</sup>, respectively. The pore size distribution curve of PANI-VOH (Figure S3b) indicates a large size ranging from 4 to 100 nm. The large pore size distribution is attributed to the stacking of the exfoliated sheets.

Figure 2c,d shows bright-field TEM analysis VOH and PANI–VOH, further highlighting the differences in their morphology. While VOH is essentially a monolithic particle,

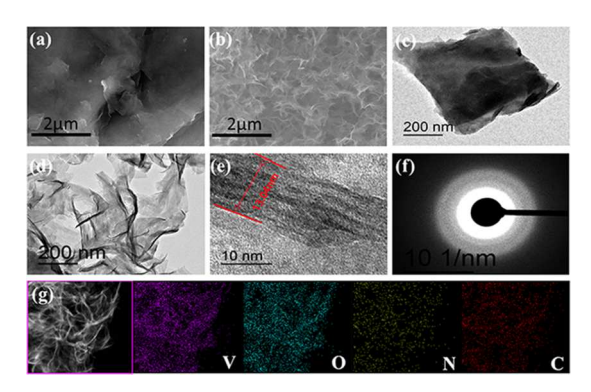


Figure 2. SEM and transmission electron microscopy (TEM) characterization of the as-synthesized PANI–VOH and baseline VOH microstructures. (a) SEM images highlighting the VOH morphology. (b) SEM images highlighting the PANI–VOH morphology. (c) TEM image further highlighting the VOH morphology. (d) TEM image further highlighting the PANI–VOH morphology. (e) HRTEM image highlighting the PANI–VOH structure. (f) Selected area electron diffraction (SAED) pattern of PANI–VOH. (g) TEM-EDXS elemental map of PANI–VOH, showing the distribution of V, O, N, and C in the material.

the PANI–VOH material is an agglomerate of nanosheets. The HRTEM analysis of PANI–VOH, shown in Figure 2e, shows its layered structure and gives the thickness of the nanosheets in the assembly. The thickness of the single nanosheet assembly is 13 nm, with 5 agglomerated nanosheets being discernable within it. Figure 2f shows the selected area electron diffraction (SAED) pattern of PANI–VOH taken from the same region as the HRTEM image. It indicates a highly nanocrystalline structure with significant peak broad-

ening due to the fine size of the crystallites. Although some lattice structure may be observed in the HRTEM images, the material is effectively diffraction amorphous. Figure 2g shows the TEM energy-dispersive X-ray spectroscopy (EDXS) elemental maps of V, O, N, and C in PANI–VOH, confirming the uniform distribution of PANI at the resolution scale of EDXS analysis. It should be pointed out that PANI is both on the surface and at the interlayers of VOH. The aniline monomers will diffuse and polymerize at the interlayers of VOH. In parallel, the aniline in solution will polymerize and absorb on the VOH surface.

Figure 3 highlights the electrochemical performance of PANI-VOH and the baseline VOH. Figure 3a shows CV curves of PANI-VOH and VOH, taken at cycle 1, tested at 0.1 mV s<sup>-1</sup> between 0.4 and 1.6 V. In baseline VOH, there is one pair of cathodic/anodic peaks, being centered at 0.97/1.1 V. These represent the reduction/oxidation V<sup>4+</sup>/V<sup>5+</sup> during intercalation/deintercalation of Zn<sup>2+</sup>. By contrast, PANI-VOH delivers four redox peaks, and these are labeled in the figure. This implies a valence state transition from V<sup>5+</sup> to V<sup>4+</sup>/  $V^{3+}$  during the multistep intercalation of  $Zn^{2+}$ . The first redox peak pair is at 0.9/0.99 V and corresponds to  $V^{5+}/V^{4+}$ . This peak pair exhibits a higher overall peak intensity and less voltage polarization than the VOH baseline, indicating more facile redox kinetics. 5,6 The other three redox peaks are at 0.76/0.78, 0.62/0.74, and 0.45/0.55 V. The redox pair of 0.76/ 0.78 V is ascribed to the protonation/deprotonation reaction in PANI along with the intercalation/deintercalation of Zn<sup>2+</sup>, both being contributors to the reversible capacity.<sup>33,34</sup> The remaining two pairs of peaks originate from further redox reaction of  $V^{5+}/V^{4+}$  and  $V^{4+}/V^{3+}$ . 2,5,6,382,5,6,38 These substantial differences in the CV behavior reveal that the introduction of

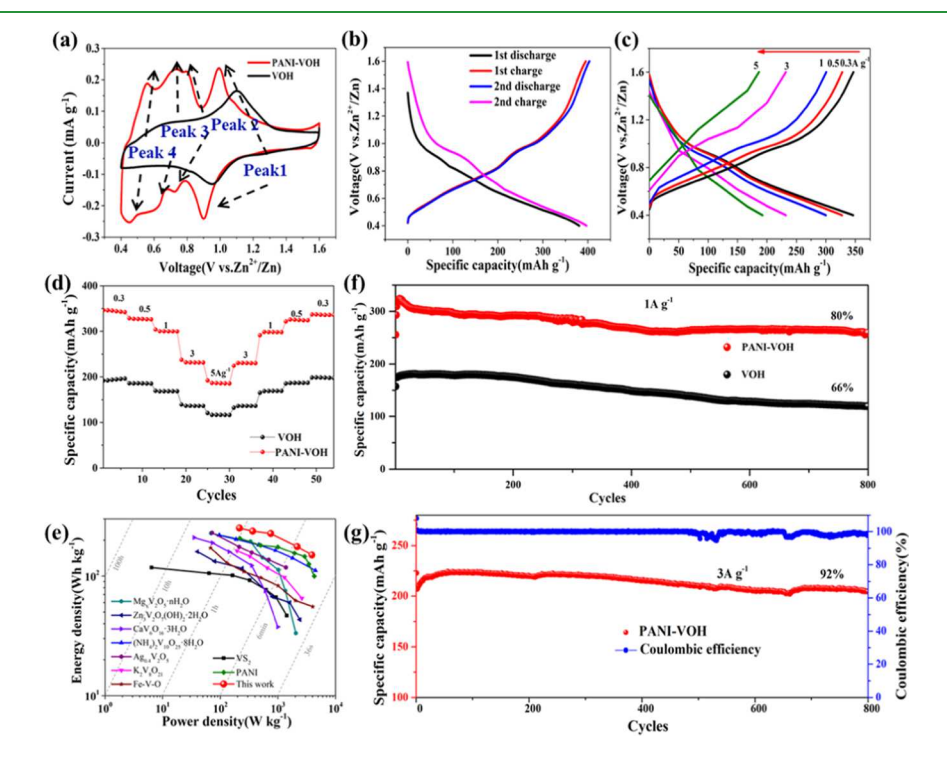


Figure 3. Electrochemical performance of PANI–VOH and baseline VOH. (a) CV curves for PANI–VOH and VOH, taken at cycle 1, tested at 0.1 mV s<sup>-1</sup> between 0.4 and 1.6 V. (b) First two galvanostatic discharge–charge curves for PANI–VOH, tested at 0.1 A g<sup>-1</sup>. (c) Galvanostatic discharge–charge curves of PANI–VOH, tested at currents ranging from 0.3 to 5 A g<sup>-1</sup>. (d) Rate performance comparison of PANI–VOH and VOH. (e) Ragone plot comparison of PANI–VOH with state-of-the-art vanadate ZIB cathodes from the literature. (f) Cycling performance of PANI–VOH and VOH, tested at 1 A g<sup>-1</sup>. (g) Cycling performance and CEs of PANI–VOH and VOH, tested at 3 A g<sup>-1</sup>.

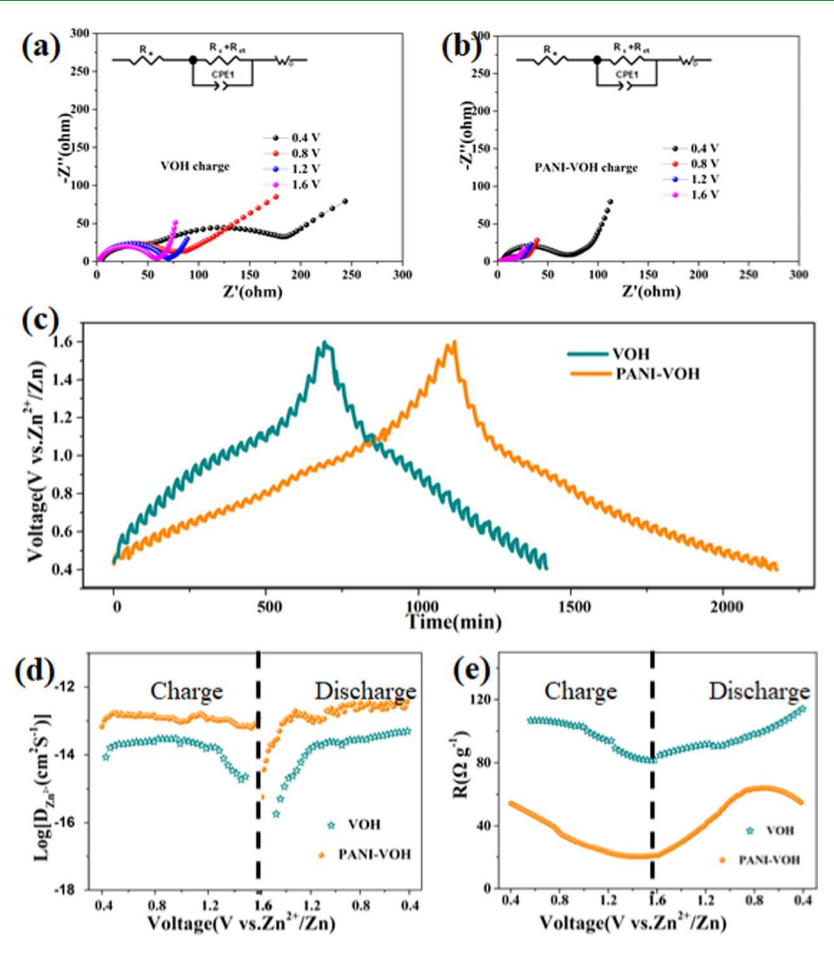


Figure 4. (a, b) EIS Nyquist plots obtained at different states of charge (voltages) for PANI–VOH and VOH, respectively. (c) GITT analysis results for PANI–VOH and VOH. (d) GITT obtained  $Zn^{2+}$  diffusion coefficient at different states of charge/discharge. (e) Internal reaction resistance (RR) of  $Zn^{2+}$  in PANI–VOH and VOH at different states of charge/discharge.

PANI facilitates the multistep conversion of  $V^{5+}/V^{4+}/V^{3+}$  and simultaneously provides additional sites for  $Zn^{2+}$  storage.

Figure 3b shows cycle 1 and two galvanostatic curves of PANI-VOH, tested at 0.1 A g<sup>-1</sup>. In both cases, the voltage plateaus are sloping, with a shift to an overall lower voltage during the second discharge. The cycle 1 and cycle 2 charge curves are nearly identical. Therefore, it appears that the main irreversible changes to the PANI-VOH structure occurred at cycle 1 discharge, whereas afterward the structure remained stable. At cycle 1, the electrode delivers discharge/charge capacities of 380/395 mAh g<sup>-1</sup>, giving a cycle 1 CE of 96%. The dQ/dV vs voltage curves reveal finer details of the redox process, not intuitively ascertained from the raw galvanostatic data. These results are shown Figure S4a, revealing two redox peak pairs, qualitatively agreeing with the CV results. The baseline VOH displays a single sloped discharge platform at about 1 V, as shown in Figure S5. This plateau is ascribed to the reversible reduction reaction of  $V^{5+}$ . The dQ/dV vs voltage curves for VOH further verify a single pair of redox peaks, as per Figure S4b. As a result, VOH only reaches a discharge/ charge capacity of 247/260 mAh g<sup>-1</sup>, with a corresponding CE of 93%.

The galvanostatic discharge—charge curves of PANI—VOH in Figure 3c show that the sloping plateau is maintained at high charge rates. By contrast, the discharge curves of VOH, shown in Figure S6, show a sharp decline without obvious plateaus. The rate performance of PANI—VOH and VOH are compared

in Figure 3d, and tests are performed at currents ranging from 0.3 to 5 A g<sup>-1</sup>. At all rates, PANI-VOH displays much higher capacities than VOH. For example, PANI-VOH obtains 346, 328, 303, 231, and 186 mAh g<sup>-1</sup> at 0.3, 0.5, 1, 3, and 5 A g<sup>-1</sup>, respectively. For VOH, these values are 190, 185, 168, 136, and 116 mAh g<sup>-1</sup> at the same currents. Figure 3e shows Ragone plots of the ZnllPANI-VOH battery, comparing it to the state-of-the-art of the Znllvanadate cathode published in the literature. The specific energy and specific power values are obtained from the galvanostatic data, and the calculated values are based on the weight of the active cathode. The ZnllPANI-VOH battery displays favorable characteristics, for example, 216 Wh kg<sup>-1</sup> at 252 W kg<sup>-1</sup>. Even at very fast charging, the battery still achieves excellent energy, e.g., 150 Wh kg<sup>-1</sup> at 3900 W kg<sup>-1</sup>. Such Ragone characteristics are favorable compared to other advanced and high-performance ZIB cathodes, such as vanadate hydrates  $(Mg_xV_2O_5\cdot nH_2O_7^6 Zn_3V_2O_7(OH)_2\cdot 2H_2O_7^{39})$ 

Figure 3f shows the extended cycling performance, tested at 1 A g $^{-1}$ . PANI $^{-1}$  VOH exhibits a reversible capacity of 255 mAh g $^{-1}$  at the first cycle, which increases to 323 mAh g $^{-1}$  after 6 cycles, presumably due to improved wetting by the electrolyte and/or material utilization. At cycle 800, PANI $^{-1}$ VOH has a reversible capacity of 259 mAh g $^{-1}$ , *i.e.*, 80% of the maximum and over 100% of the initial value. Tested at 3 A g $^{-1}$ , PANI $^{-1}$ VOH also displays 223 mAh g $^{-1}$  after 800 cycles,

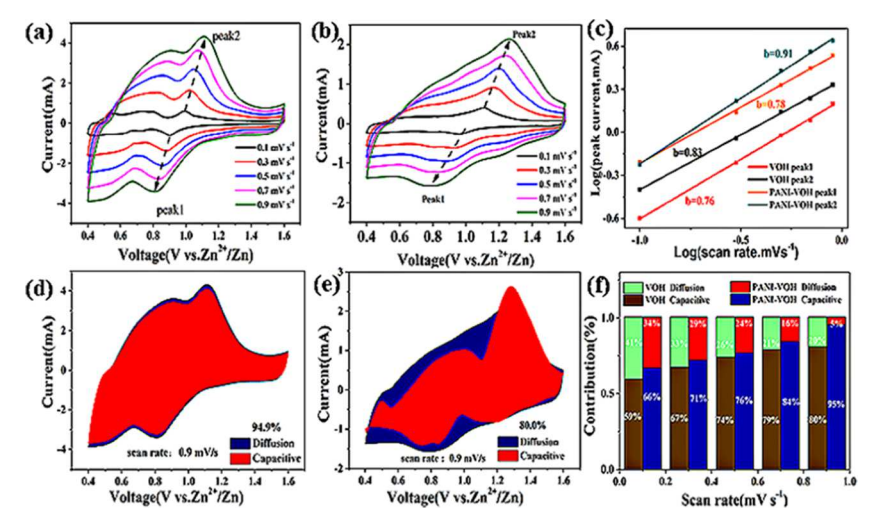


Figure 5. Electrochemical analysis of rate-limiting processes in PANI–VOH and VOH. (a, b) CV curves of PANI–VOH and VOH, obtained scan rates of 0.1, 0.3, 0.5, 0.7, and 0.9 mV s<sup>-1</sup>. (c)  $\log(v)$  vs  $\log(i)$  plots at the peak current. (d, e) Contribution ratio of diffusion-controlled vs reaction-controlled (labeled capacitive) capacities in PANI–VOH and VOH, obtained at 0.9 mV s<sup>-1</sup>. (f) Contribution ratio of diffusion-controlled vs reaction-controlled capacities at different scan rates.

corresponding to 91% capacity retention. These results are shown in Figure 3g. Figure S7 shows the associated galvanostatic charge-discharge curves for the two current densities presented at the selected cycle numbers. There is a good overlap between the galvanostatic curves even after extended cycling, indicating that the PANI-VOH microstructure remains stable. Judging from the extended stability of the PANI-VOH electrode, it does not appear that the structure is degraded to an appreciable extent. If some PANI does diffuse out, it does so only gradually during the 800 cycles, potentially being the source of the minor capacity fade observed. By contrast, after 800 cycles at 1 A g<sup>-1</sup>, VOH retains 66% of its capacity and delivers 180 mAh g<sup>-1</sup>. A comparison of cycling stability of PANI-VOH vs the most stable ZIB cathodes is shown in Table S2. Systems included in the comparison are  $V_2O_5$ , <sup>44</sup>  $V_2O_5$  composites, <sup>9,45</sup> VOH, <sup>46</sup>  $H_2V_3O_8$ ,  $^{4747}$  vanadate (LiV<sub>3</sub>O<sub>8</sub>,  $K_2V_8O_{21}$ ,  $CuV_2O_6$ ),  $^{4,48,49}$ vanadate hydrate (Li<sub>x</sub>V<sub>2</sub>O<sub>5</sub>·nH<sub>2</sub>O, Na<sub>2</sub>V<sub>6</sub>O<sub>16</sub>·1.63H<sub>2</sub>O, V<sub>3</sub>S<sub>4</sub>. <sup>59</sup> It may be observed that PANI-VOH is among the

The PANI-VOH electrokinetics were further analyzed through the use of electrochemical impedance spectroscopy (EIS) and galvanostatic intermittent titration technique (GITT) analysis. These results are shown in Figure 4a-c. For both EIS and GITT analyses, the PANI-VOH and the baseline VOH were analyzed after 30 full charge-discharge cycles performed at 0.1  ${\rm A~g^{-1}}$ . When the PANI–VOH and VOH cells were charged to different voltages (0.4, 0.8, 1.2, and 1.6 V, at 50 mA g<sup>-1</sup>), the Nyquist plots exhibit a semicircle with an inclined line. The corresponding equivalent circuit fit (inset in Figure 4a) includes contact resistance between the electrolyte and  $Zn^{2+}$  ( $R_{sol}$ ), the migrating resistance of  $Zn^{2+}$ ions through the surface layer and the charge transfer resistance  $(R_s + R_{ct})$ , surface film capacitance (CPE1), double-layer capacitance (CPE2), and the diffusion process of  $Zn^{2+}$  within the active electrode corresponding to the Warburg impedance (W). The fitted results are listed in Table S3. It may be observed that, in general, the resistance of PANI–VOH is consistently lower than that of VOH at every voltage state. For example, in the discharged state of 0.4 V, the  $R_{\rm s}+R_{\rm ct}$  of VOH is 107.5  $\Omega$ , which is twice higher than that of PANI–VOH (55.5  $\Omega$ ). At the charged state of 1.6 V, the  $R_{\rm s}+R_{\rm ct}$  of VOH is 51.2  $\Omega$ , while for PANI–VOH it is 5.3  $\Omega$ . The EIS results further support the essential role of PANI in boosting overall electrochemical kinetics of VOH, in this case, by decreasing the impedances.

Figure 4c shows the GITT analysis that was employed to evaluate the diffusion of Zn<sup>2+</sup> in the two materials. During the charge/discharge process, PANI-VOH displays a smaller IR drop at the same pulse and relaxation time. The IR drop detected from the GITT curves are transformed into ion diffusion coefficients  $D_{\rm Zn}^{\ \ 2+}$  and internal reaction resistances RR, shown in Figure 4d,e. Comparing the RR values throughout the entire charge-discharge process, it is apparent that RR for PANI-VOH is consistently half the value for VOH. The calculation details are supplied in the Supporting Information, and follow the approach by refs 30, 61-63. As shown in Figure 4d, during the discharge process, the Zn<sup>2+</sup> diffusion coefficients in the PANI-VOH range from 5.6 X  $10^{-16} \text{ cm}^2 \text{ s}^{-1}$  at 1.6 V to 3.6  $\times 10^{-13} \text{ cm}^2 \text{ s}^{-1}$  at 0.4 V. By contrast, for VOH, these range from  $1.8 \times 10^{-16}$  cm<sup>2</sup> s<sup>-1</sup> at 1.6V to  $4.9 \times 10^{-14}$  cm<sup>2</sup> s<sup>-1</sup> at 0.4 V. During the charge process,  $\rm Zn^{2+}$  diffusion coefficients in PANI–VOH are  $6.8 \times 10^{-14} \rm \ cm^2$  $s^{-1}$  at 0.4 V and 1.2  $\times$   $10^{-13}~cm^2~s^{-1}$  at 1.6 V, both values are substantially higher than in VOH under the same conditions. Both systems show a rapid increase in diffusivity at the beginning of the discharge (1.6-1.2 V), remaining relatively stable afterward (1.2 and 0.4 V). This agrees with prior reports of higher ionic diffusivity due to the deep intercalation of Zn<sup>2+,41,64</sup> Overall, the Zn<sup>2+</sup> diffusion coefficient in PANI-VOH is 10 to 100 times higher than in VOH during both charge and discharge. This may be attributed to the role of PANI and its  $\pi$ -conjugated structure, which reduces the electrostatic interactions between Zn2+ and host O2- of V-O layers. A parallel benefit of PANI, combined with the water molecules between the layers of V<sub>2</sub>O<sub>5</sub>, is to synergistically stabilize the wide Zn<sup>2+</sup> diffusion channels.<sup>28,65</sup> PANI also boosts the electrical conductivity of the electrode, allowing for

sufficient electrical charge transfer to accommodate the rapidly accumulating/depleting Zn<sup>2+</sup> in the lattice.

To further compare the reaction kinetics of Zn2+ in PANI-VOH vs VOH, CV curves were generated at different scan rates. These results are shown in Figure 5a. At scan rates from 0.1 to 0.9 mV s<sup>-1</sup>, there is a strong redox pair at 0.8/1.1 V. This pair can be evaluated to understand the redox kinetics in terms of being reaction-controlled (activation polarization) or diffusion-controlled (concentration polarization). Although activation polarization is often taken as capacitive contribution, PANI-VOH, VOH, and related systems from the published literature, the electroactive surface areas are insufficient to generate appreciable current from surface adsorption per se. Rather, what is meant by reaction-controlled in this case is a kinetically facile bulk process, where solid-state or electrolyte diffusional limitations are secondary. 66-68 Mathematically, this may be described by the following relations, originally obtained for pseudocapacitive oxides. Although the mathematical analysis remains identical, regardless of what b = 1 is taken to mean, the relatively low surface of PANI-VOH and VOH electrodes do not behave like capacitors.

$$i = av^b (1)$$

$$i(v) = k_1 v + k_2 v^{1/2} (2)$$

where i refers to the peak current cathodic or anodic currents, labeled in Figure 5a. The scan rate is v, while a and b are adjustable parameters. Figure 5c shows the calculated reduction/oxidation b values for PANI-VOH and VOH, which are 0.78/0.91 and 0.76/0.83, respectively. This indicates that both materials are reaction-controlled, although qualitatively one may argue that PANI-VOH is closer to the ideal b = 1. Figure 5d,e provides a visualization of the reactioncontrolled capacity contribution vs diffusion-controlled capacity contribution in PANI-VOH and VOH, obtained at 0.9 mV s<sup>-1</sup>. For consistency, with the published literature, the reaction-controlled contribution is labeled capacitive in the figure. The reaction-controlled proportion for PANI-VOH (94.9%) is substantially higher than that for VOH (80.0%). This difference gets even larger at higher scan rates, as may be observed from Figure 5f. These results agree with the GITT and the rate capability results, and further highlight the facile diffusion kinetics in the PANI-VOH nanosheets.

To understand the Zn<sup>2+</sup> storage mechanisms, post-mortem XRD analysis was performed on PANI-VOH at different charge/discharge voltages. When the battery discharges from the initial 1.37 to 0.9 V, the (002) peak at  $6.5^{\circ}$  for PANI-VOH becomes wider with its center shifting to a smaller angle. This may be understood in terms of the expansion of V-O layers due to Zn2+ intercalation. This process corresponds to the reduction of  $V^{5+}$  to  $V^{4+}$  and the formation of  $Zn_{0,3}V_2O_5$ . nH<sub>2</sub>O.<sup>5,6</sup> When further discharged to 0.4 V, the peak from Zn<sub>0.3</sub>V<sub>2</sub>O<sub>5</sub>·nH<sub>2</sub>O gradually decreases in intensity. Meanwhile, a sharp peak initiates at 5.8° and may be ascribed to the formation of  $Zn_xV_2O_{5-x}\cdot nH_2O$  (0.3 < x < 1.4), corresponding to further reduction of  $V^{4+}$  to  $V^{3+}$   $^{2,5,62,5,6}$ . This directly confirms that a multivalent reduction process is active in PANI-VOH. Additionally, a new peak is located at 12°, which is related to the formation of Zn<sub>3</sub>(OH)<sub>2</sub>V<sub>2</sub>O<sub>7</sub>·2H<sub>2</sub>O (PDF No. 87-0417). The formation of  $Zn_3(OH)_2V_2O_7 \cdot 2H_2O$  is ascribed to the enhanced interaction between Zn2+ and vanadium-oxygen layers accompanied by the reactions with water molecules in the aqueous electrolyte. Another new peak

near  $18^{\circ}$  may be ascribed to the formation of  $Zn_x(OTf)_y(OH)_{2x-y}\cdot nH_2O$ , per prior reports.  $^{69,70}$   $Zn_x(OTf)_y(OH)_{2x-y}\cdot nH_2O$  may form due to the reaction of  $Zn^{2+}$  with  $OTf^+$  and water, on the surface of the electrode. After being fully charged, the 8 and  $12^{\circ}$  peaks disappear. When the electrode is discharged to 0.4 V, the peaks at 5.8 and  $12^{\circ}$  are again prominent. This illustrates the reversibility of the transformation process.

Figure 6b shows the post-mortem HRTEM analysis of PANI-VOH after discharge to 0.4 V, highlighting the

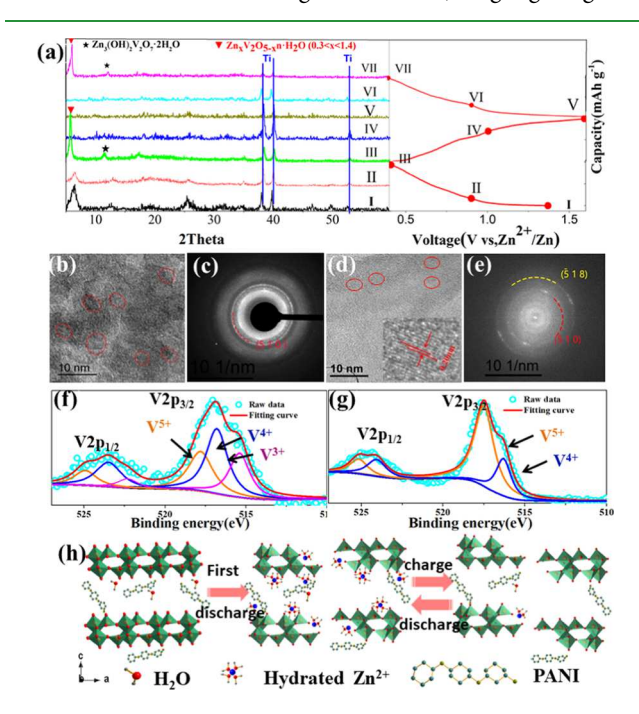


**Figure 6.** Analysis of the phase transformations in PANI–VOH galvanostatically ramped (0.1 A g<sup>-1</sup>) to different states of charge (voltage). (a) *Ex situ* XRD analysis at different states of charge, labeled I–VII. (b) HRTEM analysis of the structure after discharge to 0.4 V. (c) Associated SAED ring pattern. (d) HRTEM analysis after charging to 1.6 V. (e) Associated SAED ring pattern. (f, g) Highresolution XPS V  $2p_{1/2}$  and V  $2p_{3/2}$  spectra of fully discharged and fully charged state samples, respectively. (h) Schematic illustration of the charging and discharging reaction mechanism.

nanocrystalline structure (selected crystallites circled). According to Figure 6c, a prominent ring in the associated selected area electron diffraction (SAED) pattern corresponds to a lattice spacing of 0.231 nm and is indexed as the (510) plane of VOH (PDF No. 25-1006). The expansion of the VOH crystal structure arises from Zn<sup>2+</sup> intercalation, agreeing with the XRD results. When fully charged, PANI-VOH remains nanocrystalline, as shown in Figure 6d. According to Figure 6e, one set of lattice plane spacings is measured to be 0.20 nm, which is the (510) plane of VOH. In the SAED pattern, the two additional indexed planes of VOH are (510) and ( $\overline{5}18$ ). Examining the HRTEM results of as-synthesized vs the postdischarge/charge PANI-VOH, it can be concluded that the deep Zn2+ intercalation process causes the crystallite size refinement. This is expected to boost the electrochemical kinetics. The substantial changes in the structure would also explain the differences between the shapes of the first and the second galvanostatic curves.

Post-mortem XPS analysis was also applied to the PANI-VOH and VOH specimens at different states of charge. According to Figure 6f, when discharged to 0.4 V, PANI-VOH displays strong peaks associated with both V<sup>4+</sup> (516.8 eV) and V<sup>3+</sup> (515.4 eV),<sup>3,30</sup> in comparison to VOH (Figure S8) where these peaks are less prominent. In parallel, for PANI-VOH, the peak intensity associated with V<sup>5+</sup> (517.8 eV) is sharply decreased. However, V<sup>3+</sup> was barely detected in the VOH when discharge to 0.4 V (Figure S8a). Rather, the VOH still maintains the V<sup>5+</sup> peak (516.7 eV) after discharge to 0.4 V. When charged to 1.6 V, PANI-VOH reverts approximately the same intensity for V<sup>4+</sup>, as the as-synthesized sample analyzed by XPS and shown in Figure 1f. By contrast, there is little V<sup>4+</sup> that remains in VOH when charged back to 1.6 V, indicating some level of structural disintegration from the onset (Figure S8b). Therefore, it may be concluded that the higher reversible reduction capability of vanadium ions in PANI-VOH directly accounts for its higher reversible capacity. For N 1s of PANI in PANI-VOH, there are three peaks at 400.8, 399.2, and 398.3 eV, corresponding to the binding energies of  $-N^+=$ , -N-, and -N= at a full discharge state, respectively. Figure S9 shows those results. When battery charges from 0.4 to 1.6 V, the binding energy of -N- gradually transforms into  $-N^+=$  and -N=. This verifies that PANI is involved in the electrochemical reaction through a doping/dedoping reaction.<sup>33,3</sup>

Figure 6h illustrates the electrochemical mechanism of PANI-VOH derived from the above analytical data. During the initial discharge process, Zn2+ ions intercalate into the oxide and further expand the layered structure. Then, two new phases of  $Zn_xV_2O_{5-x}\cdot nH_2O$  (0.3 < x < 1.4) and Zn<sub>3</sub>(OH)<sub>2</sub>V<sub>2</sub>O<sub>7</sub>·2H<sub>2</sub>O are formed, both being nanocrystalline. This process is aided by the exfoliated nanosheet morphology of PANI-VOH, which reduces the solid-state diffusion distances. Meanwhile, the incorporation of PANI increases the ion solid-state diffusivity by one to two orders of magnitude, both during charge and during discharge. During the charge process, Zn2+ ions are deintercalated from  $Zn_xV_2O_{5-x}\cdot nH_2O$  (0.3 < x < 1.4) and  $Zn_3(OH)_2V_2O_7\cdot 2H_2O$ nanostructures. In the process, these phases transform back into the parent VOH structure but with a refined nanocrystalline size as well. During the subsequent charging-discharging cycling, these nanocrystalline structures remain stable, as indirectly inferred from the close overlap of the galvanostatic and CV curves after the second discharge.

# 4. CONCLUSIONS

Vanadium oxygen hydrate (VOH) cathodes for aqueous zincion batteries (ZIBs) are limited in performance due to the kinetic difficulty of reversibly intercalating Zn<sup>2+</sup> into their bulk structure. In this work, a new approach is employed to facilitate the surface charge transfer at VOH interlayers and thereby obtain improved Zn<sup>2+</sup> storage kinetics and cyclability. Polyaniline (PANI) intercalated-exfoliated VOH (termed PANI-VOH) is synthesized through the preintercalation of an aniline monomer and its in situ polymerization within the interlayers. The resulting graphene-like VOH nanosheets possess one to two orders of magnitude improved solid-state diffusivity, leading to significantly faster charging-discharging kinetics, allowing the material to undergo the full V5+ to V3+ redox reaction. In parallel, the intercalated PANI promotes enhanced structural stability of the VOH during cycling. The multielectron transform ability in PANI-VOH is ascribed to the

unique  $\pi$ -conjugated structure of PANI. It effectively alleviates electrostatic interactions between Zn<sup>2+</sup> and host O<sup>2-</sup> of V–O layers, increasing the solid-state ion diffusivity by more than an order of magnitude. PANI also stabilizes the ion diffusion channels in the oxide, while improving the ion charge transfer kinetics and electrical conductivity of the electrode.

### ASSOCIATED CONTENT

## **5** Supporting Information

The Supporting Information is available free of charge at https://pubs.acs.org/doi/10.1021/acsami.0c10183.

SEM for VOH; BET; capacity differential curve; fitted results of Nyquist plots; XPS of the N element in PANI; relative calculate methods (PDF)

#### AUTHOR INFORMATION

#### **Corresponding Authors**

Mingshan Wang — School of New Energy and Materials, Southwest Petroleum University, Chengdu, Sichuan 610500, P. R. China; ⊚ orcid.org/0000-0001-5461-3951; Email: ustbwangmingshan@163.com

David Mitlin — Materials Science and Engineering Program & Texas Materials Institute, The University of Texas at Austin, Austin, Texas 78712, United States; Email: David.Mitlin@austin.utexas.edu

Xing Li — School of New Energy and Materials, Southwest Petroleum University, Chengdu, Sichuan 610500, P. R. China; Email: lixing198141@163.com

#### **Authors**

Jun Zhang — School of New Energy and Materials, Southwest Petroleum University, Chengdu, Sichuan 610500, P. R. China Linzi Zhang — School of New Energy and Materials, Southwest Petroleum University, Chengdu, Sichuan 610500, P. R. China Jiaqi Li — School of New Energy and Materials, Southwest

Petroleum University, Chengdu, Sichuan 610500, P. R. China Wenjie Wang – School of New Energy and Materials, Southwest Petroleum University, Chengdu, Sichuan 610500, P. R. China

**Zhenliang Yang** — Institute of Materials, China Academy of Engineering Physics, Mianyang, Sichuan 621907, P. R. China

Lei Zhang – Institute of Materials, China Academy of Engineering Physics, Mianyang, Sichuan 621907, P. R. China

Yixian Wang — Materials Science and Engineering Program & Texas Materials Institute, The University of Texas at Austin, Austin, Texas 78712, United States

Junchen Chen – School of New Energy and Materials, Southwest Petroleum University, Chengdu, Sichuan 610500, P. R. China

Yun Huang — School of New Energy and Materials, Southwest Petroleum University, Chengdu, Sichuan 610500, P. R. China

Complete contact information is available at: https://pubs.acs.org/10.1021/acsami.0c10183

#### Notes

The authors declare no competing financial interest.

# **■** ACKNOWLEDGMENTS

We acknowledge the National Natural Science Foundation of China (Grant Nos. 51502250, 51604250), the Science & Technology Department of Sichuan Province (Grant Nos. 2019YFG0220, 2017JQ0044, 2019-GH02-00052-HZ), Youth Science and Technology Innovation Team of Energy Material

Electrochemistry of Southwest Petroleum University (Grant No. 2015CXTD04), and the Undergraduate Innovation Project of Science and Technology (X151519KCL03). D.M. (research guidance, manuscript preparation) and Y.W. (manuscript co-preparation) are supported by the National Science Foundation, Division of Materials Research, Award No. 1938833.

#### REFERENCES

- (1) Kundu, D.; Vajargah, S. H.; Wan, L. W.; Adams, B.; Prendergast, D.; Nazar, L. F. Aqueous vs Nonaqueous Zn-Ion Batteries: Consequences of The Desolvation Penalty at The Interface. *Energy Environ. Sci.* **2018**, *11*, 881–892.
- (2) He, P.; Zhang, G.; Liao, X.; Yan, M.; Xu, X.; An, Q.; Liu, J.; Mai, L. Sodium Ion Stabilized Vanadium Oxide Nanowire Cathode for High-Performance Zinc-Ion Batteries. *Adv. Energy Mater.* **2018**, 8, No. 1702463.
- (3) Tian, M.; Liu, C.; Zheng, J.; Jia, X.; Jahrman, E. P.; Seidler, G. T.; Long, D.; Atif, M.; Alsalhi, M.; Cao, G. Structural Engineering of Hydrated Vanadium Oxide Cathode by K<sup>+</sup> Incorporation for High-Capacity and Long-Cycling Aqueous Zinc Ion Batteries. *Energy Storage Mater.* **2020**, *29*, 9–16.
- (4) Tang, B.; Fang, G.; Zhou, J.; Wang, L.; Lei, Y.; Wang, C.; Lin, T.; Tang, Y.; Liang, S. Potassium Vanadates with Stable Structure and Fast Ion Diffusion Channel as Cathode for Rechargeable Aqueous Zinc-Ion Batteries. *Nano Energy* **2018**, *51*, 579–587.
- (5) Kundu, D.; Adams, B. D.; Duffort, V.; Vajargah, S. H.; Nazar, L. F. A High-Capacity and Long-Life Aqueous Rechargeable Zinc Battery Using a Metal Oxide Intercalation Cathode. *Nat. Energy* **2016**, *1*, No. 16119.
- (6) Ming, F.; Liang, H.; Lei, Y.; Kandambeth, S.; Eddaoudi, M.; Alshareef, H. N. Layered Mg<sub>x</sub>V<sub>2</sub>O<sub>5</sub>·nH<sub>2</sub>O as Cathode Material for High-Performance Aqueous Zinc Ion Batteries. *ACS Energy Lett.* **2018**, 3, 2602–2609.
- (7) Xia, C.; Guo, J.; Li, P.; Zhang, X.; Alshareef, H. N. Highly Stable Aqueous Zinc-Ion Storage Using a Layered Calcium Vanadium Oxide Bronze Cathode. *Angew. Chem., Int. Ed.* **2018**, *57*, 3943–3948.
- (8) Qian, L.; Wei, T.; Ma, K.; Yang, G.; Wang, C. Boosting the Cyclic Stability of Aqueous Zinc-Ion Battery Based on Al-Doped V<sub>10</sub>O<sub>24</sub>·12H<sub>2</sub>O Cathode Materials. *ACS Appl. Mater. Interfaces* **2019**, 11, 20888–20894.
- (9) Yan, M.; He, P.; Chen, Y.; Wang, S.; Wei, Q.; Zhao, K.; Xu, X.; An, Q.; Shuang, Y.; Shao, Y.; Mueller, K. T.; Mai, L.; Liu, J.; Yang, J. Water-Lubricated Intercalation in  $V_2O_5$ .n $H_2O$  for High-Capacity and High-Rate Aqueous Rechargeable Zinc Batteries. *Adv. Mater.* **2018**, 30, No. 1703725.
- (10) Xu, X.; Xiong, F.; Meng, J.; Wang, X.; Niu, C.; An, Q.; Mai, L. Vanadium-Based Nanomaterials: A Promising Family for Emerging Metal-Ion Batteries. *Adv. Funct. Mater.* **2020**, *30*, No. 1904398.
- (11) Tang, B.; Shan, L.; Liang, S.; Zhou, J. Issues and Opportunities Facing Aqueous Zinc-Ion Batteries. *Energy Environ. Sci.* **2019**, *12*, 3288–3304.
- (12) Blanc, L. E.; Kundu, D.; Nazar, L. F. Scientific Challenges for The Implementation of Zn-Ion Batteries. *Joule* **2020**, *4*, 771–799.
- (13) Zeng, X.; Hao, J.; Wang, Z.; Mao, J.; Guo, Z. Recent Progress and Perspectives on Aqueous Zn-Based Rechargeable Batteries with Mild Aqueous Electrolytes. *Energy Storage Mater.* **2019**, *20*, 410–437.
- (14) Yamamoto, T.; Shoji, T. Rechargeable ZnlZnSO<sub>4</sub>lMnO<sub>2</sub>-Type Cells. *Inorg. Chim. Acta* **1986**, 117, L27–L28.
- (15) Song, M.; Tan, H.; Chao, D.; Fan, H. J. Recent Advances in Zn-Ion Batteries. *Adv. Funct. Mater.* **2018**, 28, No. 1802564.
- (16) Cao, A. M.; Hu, J. S.; Liang, H. P.; Wan, L. J. Self-Assembled Vanadium Pentoxide ( $V_2O_5$ ) Hollow Microspheres From Nanorods and Their Application in Lithium-Ion Batteries. *Angew. Chem., Int. Ed.* **2005**, *44*, 4391–4395.
- (17) Moretti, A.; Secchiaroli, M.; Buchholz, D.; Giuli, G.; Marassi, R.; Passerini, S. Exploring the Low Voltage Behavior of  $V_2O_5$  Aerogel

- as Intercalation Host for Sodium Ion Battery. J. Electrochem. Soc. 2015, 162, A2723—A2728.
- (18) Su, D.; Wang, G. Single-Crystalline Bilayered  $\rm V_2O_5$  Nanobelts for High-Capacity Sodium-Ion Batteries. ACS Nano 2013, 7, 11218–11226.
- (19) Li, Y.; Huang, Z.; Kalambate, P. K.; Zhong, Y.; Huang, Z.; Xie, M.; Shen, Y.; Huang, Y. V<sub>2</sub>O<sub>5</sub> Nanopaper as a Cathode Material with High Capacity and Long Cycle Life for Rechargeable Aqueous Zinc-Ion Battery. *Nano Energy* **2019**, *60*, 752–759.
- (20) Senguttuvan, P.; Han, S.-D.; Kim, S.; Lipson, A. L.; Tepavcevic, S.; Fister, T. T.; Bloom, I. D.; Burrell, A. K.; Johnson, C. S. A High Power Rechargeable Nonaqueous Multivalent Zn/V<sub>2</sub>O<sub>5</sub> Battery. *Adv. Energy Mater.* **2016**, *6*, No. 1600826.
- (21) Shan, L.; Zhou, J.; Zhang, W.; Xia, C.; Guo, S.; Ma, X.; Fang, G.; Wu, X.; Liang, S. Highly Reversible Phase Transition Endows  $V_6O_{13}$  with Enhanced Performance as Aqueous Zinc-Ion Battery Cathode. *Energy Technol.* **2019**, *7*, No. 1900022.
- (22) Shan, L.; Yang, Y.; Zhang, W.; Chen, H.; Fang, G.; Zhou, J.; Liang, S. Observation of Combination Displacement/Intercalation Reaction in Aqueous Zinc-Ion Battery. *Energy Storage Mater.* **2019**, *18*, 10–14.
- (23) Huang, P.; Ling, W.; Sheng, H.; Zhou, Y.; Wu, X.; Zeng, X.-X.; Wu, X.; Guo, Y.-G. Heteroatom-Doped Electrodes for All-Vanadium Redox Flow Batteries with Ultralong Lifespan. *J. Mater. Chem. A* **2018**, *6*, 41–44.
- (24) Liao, M.; Wang, J.; Ye, L.; Sun, H.; Wen, Y.; Wang, C.; Sun, X.; Wang, B.; Peng, H. A Deep-Cycle Aqueous Zinc-Ion Battery Containing an Oxygen-Deficient Vanadium Oxide Cathode. *Angew. Chem., Int. Ed.* **2020**, *59*, 2273–2278.
- (25) Suo, L.; 1 Borodin, O.; Gao, T.; Olguin, M.; Ho, J.; Fan, X.; Luo, C.; Wang, C.; Xu, K. "Water-In-Salt" Electrolyte Enables High-Voltage Aqueous Lithium-Ion Chemistries. *Science* **2015**, *350*, 938–943.
- (26) Kundu, D.; Vajargah, S. H.; Wan, L.; Adams, B.; Prendergastb, D.; Nazar, L. F. Aqueous vs Nonaqueous Zn-Ion Batteries: Consequences of The Desolvation Penalty at The Interface. *Energy Environ. Sci.* **2018**, *11*, 881–892.
- (27) Shin, J.; Choi, D. S.; Lee, H. J.; Jung, Y.; Choi, J. W. Hydrated Intercalation for High-Performance Aqueous Zinc Ion Batteries. *Adv. Energy Mater.* **2019**, *9*, No. 1900083.
- (28) Huang, J.; Wang, Z.; Hou, M.; Dong, X.; Liu, Y.; Wang, Y.; Xia, Y. Polyaniline-Intercalated Manganese Dioxide Nanolayers as a High-Performance Cathode Material for an Aqueous Zinc-Ion Battery. *Nat. Commun.* **2018**, *9*, No. 2906.
- (29) Zhou, L.; Liu, Q.; Zhang, Z.; Zhang, K.; Xiong, F.; Tan, S.; An, Q.; Kang, Y. M.; Zhou, Z.; Mai, L. Interlayer-Spacing-Regulated VOPO<sub>4</sub> Nanosheets with Fast Kinetics for High-Capacity and Durable Rechargeable Magnesium Batteries. *Adv. Mater.* **2018**, *30*, No. 1801984.
- (30) Liu, C.; Neale, Z.; Zheng, J.; Jia, X.; Huang, J.; Yan, M.; Tian, M.; Wang, M.; Yang, J.; Cao, G. Expanded Hydrated Vanadate for High-Performance Aqueous Zinc-Ion Batteries. *Energy Environ. Sci.* **2019**, *12*, 2273–2285.
- (31) Wang, M.-S.; Wang, Z.-Q.; Chen, Z.; Yang, Z.-L.; Tang, Z.-L.; Luo, H.-Y.; Huang, Y.; Li, X.; Xu, W. One Dimensional and Coaxial Polyaniline@Tin dioxide@Multi-wall Carbon Nanotube as Advanced Conductive Additive Free Anode for Lithium Ion Battery. *Chem. Eng. J.* 2018, 334, 162–171.
- (32) Dong, J.; Jiang, Y.; Wei, Q.; Tan, S.; Xu, Y.; Zhang, G.; Liao, X.; Yang, W.; Li, Q.; An, Q.; Mai, L. Strongly Coupled Pyridine- $V_2O_5$ ·nHO Nanowires with Intercalation Pseudocapacitance and Stabilized Layer for High Energy Sodium Ion Capacitors. *Small* **2019**, *15*, No. 1900379.
- (33) Cao, H.; Wan, F.; Zhang, L.; Dai, X.; Huang, S.; Liu, L.; Niu, Z. Highly Compressible Zinc-Ion Batteries with Stable Performance. *J. Mater. Chem. A* **2019**, *7*, 11734–11741.
- (34) Shi, H. Y.; Ye, Y. J.; Liu, K.; Song, Y.; Sun, X. A Long-Cycle-Life Self-Doped Polyaniline Cathode for Rechargeable Aqueous Zinc Batteries. *Angew. Chem., Int. Ed.* **2018**, *57*, 16359–16363.

- (35) Lee, J.; Badie, S.; Srimuk, P.; Ridder, A.; Shim, H.; Choudhury, S.; Nah, Y.-C.; Presser, V. Electrodeposition of Hydrated Vanadium Pentoxide on Nanoporous Carbon Cloth for Hybrid Energy Storage. *Sustainable Energy Fuels* **2018**, *2*, 577–588.
- (36) Boukhalfa, S.; Evanoff, K.; Yushin, G. Atomic Layer Deposition of Vanadium Oxide on Carbon Nanotubes for High-Power Supercapacitor Electrodes. *Energy Environ. Sci.* **2012**, *5*, 6872.
- (37) Gawli, Y.; Banerjee, A.; Dhakras, D.; Deo, M.; Bulani, D.; Wadgaonkar, P.; Shelke, M.; Ogale, S. 3D Polyaniline Architecture by Concurrent Inorganic and Organic Acid Doping for Superior and Robust High Rate Supercapacitor Performance. *Sci. Rep.* **2016**, *6*, No. 21002.
- (38) Tang, B.; Zhou, J.; Fang, G.; Liu, F.; Zhu, C.; Wang, C.; Pan, A.; Liang, S. Engineering the Interplanar Spacing of Ammonium Vanadates as a High-Performance Aqueous Zinc-Ion Battery Cathode. *J. Mater. Chem. A* **2019**, *7*, 940–945.
- (39) Xia, C.; Guo, J.; Lei, Y.; Liang, H.; Zhao, C.; Alshareef, H. N. Rechargeable Aqueous Zinc-Ion Battery Based on Porous Framework Zinc Pyrovanadate Intercalation Cathode. *Adv. Mater.* **2018**, *30*, No. 1705580.
- (40) Liu, X.; Zhang, H.; Geiger, D.; Han, J.; Varzi, A.; Kaiser, U.; Moretti, A.; Passerini, S. Calcium Vanadate Sub-Microfibers as Highly Reversible Host Cathode Material for Aqueous Zinc-Ion Batteries. *Chem. Commun.* **2019**, *55*, 2265–2268.
- (41) Wei, T.; Li, Q.; Yang, G.; Wang, C. Highly Reversible and Long-Life Cycling Aqueous Zinc-Ion Battery Based on Ultrathin (NH<sub>4</sub>)<sub>2</sub>V<sub>10</sub>O<sub>25</sub>·8H<sub>2</sub>O Nanobelts. *J. Mater. Chem. A* **2018**, *6*, 20402–20410.
- (42) Luo, Y.; Wei, L.; Geng, H.; Zhang, Y.; Yang, Y.; Li, C. C. Amorphous Bimetallic Oxides Fe-V-O with Tunable Compositions toward Rechargeable Zn-Ion Batteries with Excellent Low-Temperature Performance. ACS Appl. Mater. Interfaces 2020, 12, 11753—11760.
- (43) Pu, X.; Song, T.; Tang, L.; Tao, Y.; Cao, T.; Xu, Q.; Liu, H.; Wang, Y.; Xia, Y. Rose-Like Vanadium Disulfide Coated by Hydrophilic Hydroxyvanadium Oxide with Improved Electrochemical Performance as Cathode Material for Aqueous Zinc-Ion Batteries. *J. Power Sources* **2019**, 437, No. 226917.
- (44) Chen, X.; Wang, L.; Li, H.; Cheng, F.; Chen, J. Porous  $\rm V_2O_5$  Nanofibers as Cathode Materials for Rechargeable Aqueous Zinc-Ion Batteries. *J. Energy Chem.* **2019**, 38, 20–25.
- (45) Xu, D.; Wang, H.; Li, F.; Guan, Z.; Wang, R.; He, B.; Gong, Y.; Hu, X. Conformal Conducting Polymer Shells on V<sub>2</sub>O<sub>5</sub> Nanosheet Arrays as a High-Rate and Stable Zinc-Ion Battery Cathode. *Adv. Mater. Interfaces* **2019**, *6*, No. 1801506.
- (46) Liu, W.; Dong, L.; Jiang, B.; Huang, Y.; Wang, X.; Xu, C.; Kang, Z.; Mou, J.; Kang, F. Layered Vanadium Oxides with Proton and Zinc Ion Insertion for Zinc Ion Batteries. *Electrochim. Acta* **2019**, 320, 134565–134573.
- (47) He, P.; Quan, Y.; Xu, X.; Yan, M.; Yang, W.; An, Q.; He, L.; Mai, L. High-Performance Aqueous Zinc-Ion Battery Based on Layered H<sub>2</sub>V<sub>3</sub>O<sub>8</sub> Nanowire Cathode. *Small* **2017**, *13*, No. 1702551.
- (48) Alfaruqi, M. H.; Mathew, V.; Song, J.; Kim, S.; Islam, S.; Pham, D. T.; Jo, J.; Kim, S.; Baboo, J. P.; Xiu, Z.; Lee, K. S.; Sun, Y. K.; Kim, J. Electrochemical Zinc Intercalation in Lithium Vanadium Oxide: A High-Capacity Zinc-Ion Battery Cathode. *Chem. Mater.* **2017**, *29*, 1684–1694.
- (49) Yu, X.; Hu, F.; Cui, F.; Zhao, J.; Guan, C.; Zhu, K. The Displacement Reaction Mechanism of The  $\text{CuV}_2\text{O}_6$  Nanowire Cathode for Rechargeable Aqueous Zinc Ion Batteries. *Dalton Trans.* **2020**, *49*, 1048–1055.
- (50) Yang, Y.; Tang, Y.; Fang, G.; Shan, L.; Guo, J.; Zhang, W.; Wang, C.; Wang, L.; Zhou, J.; Liang, S. Li<sup>+</sup> Intercalated V<sub>2</sub>O<sub>5</sub>·nH<sub>2</sub>O with Enlarged Layer Spacing and Fast Ion Diffusion as an Aqueous Zinc-Ion Battery Cathode. *Energy Environ. Sci.* **2018**, *11*, 3157–3162.
- (51) Hu, P.; Zhu, T.; Wang, X.; Wei, X.; Yan, M.; Li, J.; Luo, W.; Yang, W.; Zhang, W.; Zhou, L.; Zhou, Z.; Mai, L. Highly Durable  $Na_2V_6O_{16}\cdot 1.63H_2O$  Nanowire Cathode for Aqueous Zinc-Ion Battery. *Nano Lett.* **2018**, *18*, 1758–1763.

- (52) Sambandam, B.; Soundharrajan, V.; Kim, S.; Alfaruqi, M. H.; Jo, J.; Kim, S.; Mathew, V.; Sun, Y.-k.; Kim, J.  $K_2V_6O_{16}\cdot 2.7H_2O$  Nanorod Cathode: An Advanced Intercalation System for High Energy Aqueous Rechargeable Zn-Ion Batteries. *J. Mater. Chem. A* **2018**, *6*, 15530–15539.
- (53) Liu, X.; Zhang, H.; Geiger, D.; Han, J.; Varzi, A.; Kaiser, U.; Moretti, A.; Passerini, S. Calcium Vanadate Sub-Microfibers as Highly Reversible Host Cathode Material for Aqueous Zinc-Ion Batteries. *Chem. Commun.* **2019**, *55*, 2265–2268.
- (54) Peng, Z.; Wei, Q.; Tan, S.; He, P.; Luo, W.; An, Q.; Mai, L. Novel Layered Iron Vanadate Cathode for High-Capacity Aqueous Rechargeable Zinc Batteries. *Chem. Commun.* **2018**, *54*, 4041–4044.
- (55) Shi, H. Y.; Song, Y.; Qin, Z.; Li, C.; Guo, D.; Liu, X. X.; Sun, X. Inhibiting VOPO<sub>4</sub>xH<sub>2</sub>O Decomposition and Dissolution in Rechargeable Aqueous Zinc Batteries to Promote Voltage and Capacity Stabilities. *Angew. Chem., Int. Ed.* **2019**, *58*, 16057–16061.
- (56) Li, G.; Yang, Z.; Jiang, Y.; Jin, C.; Huang, W.; Ding, X.; Huang, Y. Towards Polyvalent Ion Batteries: A Zinc-Ion Battery Based on NASICON Structured Na<sub>3</sub>V<sub>2</sub>(PO<sub>4</sub>)<sub>3</sub>. *Nano Energy* **2016**, 25, 211–217.
- (57) Ding, J.; Du, Z.; Gu, L.; Li, B.; Wang, L.; Wang, S.; Gong, Y.; Yang, S. Ultrafast Zn<sup>2+</sup> Intercalation and Deintercalation in Vanadium Dioxide. *Adv. Mater.* **2018**, *30*, No. 1800762.
- (58) He, P.; Yan, M.; Zhang, G.; Sun, R.; Chen, L.; An, Q.; Mai, L. Layered VS<sub>2</sub> Nanosheet-Based Aqueous Zn Ion Battery Cathode. *Adv. Energy Mater.* **2017**, *7*, No. 1601920.
- (59) Liu, S.; Chen, X.; Zhang, Q.; Zhou, J.; Cai, Z.; Pan, A. Fabrication of an Inexpensive Hydrophilic Bridge on a Carbon Substrate and Loading Vanadium Sulfides for Flexible Aqueous Zinc-Ion Batteries. ACS Appl. Mater. Interfaces 2019, 11, 36676–36684.
- (60) He, P.; Yan, M. Y.; Liao, X. B.; Mai, L. Q.; Nan, C.-W.; Luo, Y. Reversible V<sup>3+</sup>/V<sup>5+</sup> Double Redox in Lithium Vanadium Oxide Cathode for Zinc Storage. *Energy Storage Mater.* **2020**, *29*, 113–120.
- (61) Shen, Z.; Cao, L.; Rahn, C. D.; Wang, C.-Y. Least Squares Galvanostatic Intermittent Titration Technique (LS-GITT) for Accurate Solid Phase Diffusivity Measurement. *J. Electrochem. Soc.* **2013**, *160*, A1842—A1846.
- (62) Dees, D. W.; Kawauchi, S.; Abraham, D. P.; Prakash, J. Analysis of the Galvanostatic Intermittent Titration Technique (GITT) as Applied to a Lithium-Ion Porous Electrode. *J. Power Sources* **2009**, 189, 263–268.
- (63) Zhu, Y.; Wang, C. Galvanostatic Intermittent Titration Technique for Phase-Transformation Electrodes. *J. Phys. Chem. C* **2010**, *114*, 2830–2841.
- (64) Geng, H.; Cheng, M.; Wang, B.; Yang, Y.; Zhang, Y.; Li, C. C. Electronic Structure Regulation of Layered Vanadium Oxide via Interlayer Doping Strategy toward Superior High-Rate and Low-Temperature Zinc-Ion Batteries. *Adv. Funct. Mater.* **2020**, 30, No. 1907684.
- (65) Wan, F.; Zhang, L.; Wang, X.; Bi, S.; Niu, Z.; Chen, J. An Aqueous Rechargeable Zinc-Organic Battery with Hybrid Mechanism. *Adv. Funct. Mater.* **2018**, 28, No. 1804975.
- (66) Ding, J.; Zhang, H.; Zhou, H.; Feng, J.; Zheng, X.; Zhong, C.; Paek, E.; Hu, W.; Mitlin, D. Sulfur-Grafted Hollow Carbon Spheres for Potassium-Ion Battery Anodes. *Adv. Mater.* **2019**, *31*, No. 1900429.
- (67) Lee, B.; Kim, M.; Kim, S.; Nanda, J.; Kwon, S. J.; Jang, H. D.; Mitlin, D.; Lee, S. W. High Capacity Adsorption-Dominated Potassium and Sodium Ion Storage in Activated Crumpled Graphene. *Adv. Energy Mater.* **2020**, *10*, No. 1903280.
- (68) Tao, L.; Yang, Y.; Wang, H.; Zheng, Y.; Hao, H.; Song, W.; Shi, J.; Huang, M.; Mitlin, D. Sulfur-Nitrogen Rich Carbon as Stable High Capacity Potassium Ion Battery Anode: Performance and Storage Mechanisms. *Energy Storage Mater.* **2020**, 27, 212–225.
- (69) Liu, Y.; Li, Q.; Ma, K.; Yang, G.; Wang, C. Graphene Oxide Wrapped  $\text{CuV}_2\text{O}_6$  Nanobelts as High-Capacity and Long-Life Cathode Materials of Aqueous Zinc-Ion Batteries. *ACS Nano* **2019**, 13, 12081–12089.

(70) Wei, T.; Li, Q.; Yang, G.; Wang, C. Pseudo-Zn-Air and Zn-Ion Intercalation Dual Mechanisms to Realize High-Areal Capacitance and Long-Life Energy Storage in Aqueous Zn Battery. *Adv. Energy Mater.* **2019**, *9*, No. 1901480.